Takagi *et al. Earth, Planets and Space* (2019) 71:124
https://doi.org/10.1186/s40623-019-1103-x

Earth, Planets and Space

FULL PAPER Open Access

An uppermost haze layer above 100 km found over Venus by the SOIR instrument onboard Venus Express

Seiko Takagi[1*], Arnaud Mahieux[2,3], Valérie Wilquet[2], Séverine Robert[2], Ann Carine Vandaele[2] and Naomoto Iwagami[4]

Abstract

The Solar Occultation in the InfraRed (SOIR) instrument onboard Venus Express was designed to measure the Venusian atmospheric transmission at high altitudes (65–220 km) in the infrared range (2.2–4.3 μm) with a high spectral resolution. In this work, we investigate the optical properties of Venus's haze layer above 90 km using SOIR solar occultation observations. Vertical and latitudinal profiles of the extinction coefficient, optical thickness, and mixing ratio of aerosols are retrieved. One of the most remarkable results is that the aerosol mixing ratio tends to increase with altitude above 90 km at both high and low latitudes. We speculate how aerosols could be produced at such high altitudes.

Keywords: Venus, Cloud, Haze, Atmosphere, Spectroscopy

Introduction

The clouds above Venus consist of a main cloud deck located between approx. 47 and 70 km surrounded by thinner hazes above and below. The upper haze layer was observed at altitudes as high as 90 km (Esposito et al. 1983). The presence of high-altitude hazes/aerosols was also inferred from the analysis of limb profiles observed by the Venus Monitoring Camera (VMC) onboard ESA's Venus Express (Vex) (Limaye et al. 2015) and from SPICAV-IR and UV solar occultations (Luginin et al. 2016). The mean particle radius (~1 μm) within the cloud layer was previously determined from polarimetry observations in the early 1970s (Hansen and Hovenier 1974). These particles are most likely composed of concentrated sulfuric acid (Esposito 1984), as deduced from refractive index measurements. The existence of smaller particles within and above the clouds with an effective radius of 0.23 ± 0.04 μm and a refractive index of 1.45 ± 0.04 was suggested from Pioneer Venus Orbiter (PVO) Cloud Photopolarimeter measurements at 550 nm (Kawabata et al. 1980). From PVO Cloud Photopolarimeter observations, Sato et al. (1996) reported that these haze particles have an effective radius of 0.25 ± 0.05 μm and a refractive index of 1.435 ± 0.02 in the North Pole region; in the South Pole region, these haze particles have an effective radius of 0.29 ± 0.02 μm and a refractive index of 1.45 ± 0.02. The haze optical thickness above the clouds in the polar regions was found to be equal to 0.8 at 365 nm but only 0.06 at low latitudes (Kawabata et al. 1980). In Takagi and Iwagami (2011), the cloud optical thickness, which includes the optical thickness of the haze layer, was estimated from data collected by the previous entry probes, such as the Soviet Venera series; the haze optical thickness from 70 to 90 km at 920 nm was found to be 1.0. Vertical extinction profiles were obtained from data acquired over several wavelengths in the UV and IR domains with SPICAV/SOIR instruments (Wilquet et al. 2009). The extinction values differ according to different wavelengths. The optical properties of aerosols have been inferred from their wavelength dependence. Long-term temporal variations in the haze layer were investigated using PVO cloud photopolarimeter observation data (Braak et al. 2002); a gradual decrease

*Correspondence: seiko@ep.sci.hokudai.ac.jp
[1] Department of Earth and Planetary Sciences, Hokkaido University, Faculty of Science, Kita 10, Nishi 8, Kita-ku, Sapporo 060-0810, Japan
Full list of author information is available at the end of the article

in the haze particle column density was observed during the Pioneer Venus mission. The haze optical thickness was found to be 0.25 in 1978 and 0.1 or less in 1990. From PVO Cloud Photopolarimeter observation data, Sato et al. (1996) also showed short-term temporal variations in the haze optical thickness in the polar regions. As shown in Belyaev et al. (2008), after a sharp increase in the SO_2 abundance between 1967 and 1979, a gradual decrease in the SO_2 abundance beginning in 1995 was observed. Several possible explanations of such variations were later considered by Mills and Allen (2007). More recently, another global increase in the SO_2 abundance between 2004 and 2007 was observed (Belyaev et al. 2008). Esposito et al. (1988) reported a correlation coefficient of 0.8 between the SO_2 abundance and polar haze optical thickness from PVO Cloud Photopolarimeter observations. However, it is still unclear how hazes are produced and what their composition is.

The haze optical properties up to 90 km were presented in Wilquet et al. (2009, 2012), who also described an analysis of spectra from the SOIR instrument, a high-resolution infrared echelle spectrometer onboard Venus Express. Wilquet et al. (2012) reported that the aerosol extinction coefficient is significantly smaller at high latitudes (at least by a factor 10) than in the equatorial region. Wilquet et al. (2009) also showed the existence of at least two types of particles with radii of ~0.1–0.3 μm and ~0.4–1.0 μm depending on the altitude. On the other hand, the SO and SO_2 mixing ratios were shown to increase with the altitude from 85 to 105 km (Belyaev et al. 2012; Mahieux et al. 2015b). These observations were tentatively explained by the existence of a still unknown source of SO and SO_2 at high altitudes. One possible source could be the photodissociation of SO_3, which results from the evaporation of H_2SO_4 droplets. For example, Zhang et al. (2012) showed important chemical pathways for sulfur species related to aerosols. Additionally, it has been speculated that aerosols and sulfur compounds are connected by condensation and evaporation (Zhang et al. 2012). However, upper limit measurements of H_2SO_4 using submillimeter ground-based observations make this suggestion unlikely (Sandor et al. 2012). Clearly, what occurs above 90 km is not yet understood.

Venus Express, the first European mission to Venus, was intended to provide a global investigation of the atmosphere and plasma environment above Venus (Svedhem et al. 2007). The spacecraft was launched on November 2005 from Baikonur, Kazakhstan, arrived at Venus on April 2006, and continued operating for more than 8 years. It was inserted in an elliptical orbit; its perigee was above the North Pole (~ 250 km), and its perigee was above the South Pole (~ 66,000 km). The satellite's orbital period was 24 Earth hours. Several instruments on the Venus Express spacecraft were able to observe the Venus atmosphere over a broad range of wavelengths. VMC images have also been used to infer some results on hazes via estimates of the slant unit optical depth from limb determinations at four visible/near-infrared wavelengths (Limaye et al. 2015). The Visible and Infrared Thermal Imaging Spectrometer (VIRTIS-M IR) (de Kok et al. 2011) and Spectroscopy for the Investigation of the Characteristics of the Atmosphere of Venus/Solar Occultation at InfraRed (SPICAV/SOIR) (Wilquet et al. 2009) instruments were able to investigate the upper haze layer above the clouds on the night side. The aim of this study is to examine the haze optical properties above that altitude by analyzing SOIR data to understand the processes at play at such high altitudes.

Description of the observations

The SOIR instrument

SOIR, one of the three channels of the SPICAV/SOIR instrument (Bertaux et al. 2007) onboard Venus Express, is a compact and high-resolution IR echelle grating spectrometer working at high diffraction orders (simply called orders hereafter) between 101 and 194 (Nevejans et al. 2006). More details on the instrument can be found in Nevejans et al. (2006), Mahieux et al. (2008, 2009) and Vandaele et al. (2013); only a summary is given here. The SOIR instrument operates in the IR domain [2.2–4.3 μm (2200 cm^{-1}–4400 cm^{-1})], and its spectral resolution varies between 0.1 and 0.19 cm^{-1}. The free spectral range is equal to 24 cm^{-1}. An acousto-optical tunable filter (AOTF) was placed beyond the optical entrance of the instrument to select the echelle diffraction orders to be measured during an occultation, and it was designed to have a full width at half maximum (FWHM) of 24 cm^{-1}. Four orders are recorded simultaneously during an occultation. The detector pixels are summed on board in the spatial direction to form two bins; this means that the spectral resolution is lowered by a factor of two by binning. The vertical resolution varies between 200 and 700 m when measuring at high northern latitudes and between 2 and 5 km in the Southern Hemisphere (Mahieux et al. 2010). The observed spectra at northern latitudes have a high vertical resolution compared to those observed at southern latitudes due to the elliptical orbit of the satellite with its perigee above the North Pole.

SOIR always operated in solar occultation mode, i.e., the instrument's line of sight (LOS) was pointed towards the Sun. Figure 1 shows the geometry of a solar occultation observation. Solar occultation is a technique in which the spectra are obtained by dividing the spectra measured while looking at the Sun through the Venus atmosphere by an exoatmospheric reference spectrum

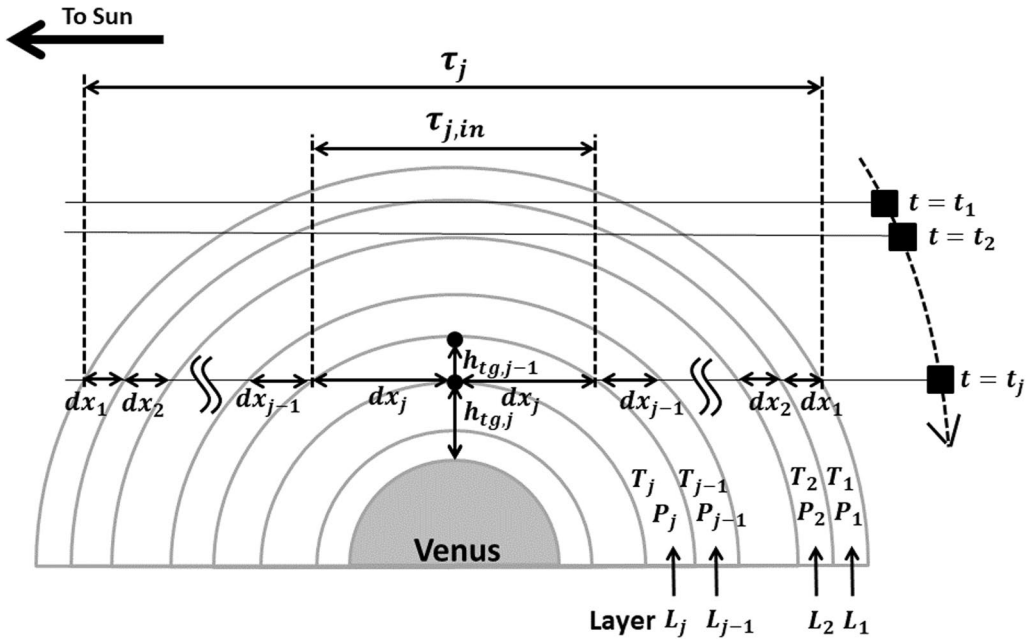

Fig. 1 Geometry of solar occultation measurements and the analysis method in this study (modified from Fig. 4 of Vandaele et al. 2008). In the ingress case depicted here, the instrument is taking a measurement every second. The tangent altitude $h_{tg,j}$ defines the layers in the atmosphere. In each layer L_i, the temperature T_i and pressure P_i are assumed to be constant

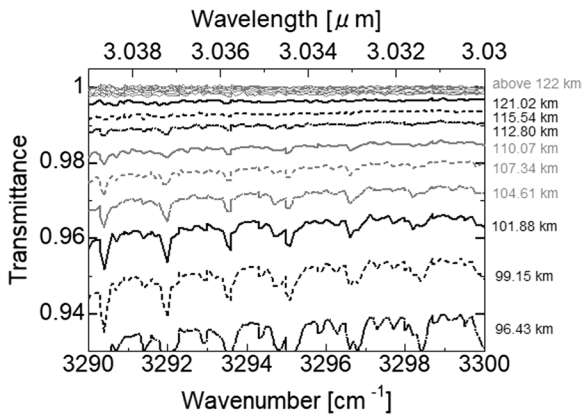

Fig. 2 Example of observed transmittances (Dec. 03, 2007, order 147, orbit 591, latitude 9°S, longitude 209°) above an altitude of 95 km. These wavelengths are selected to visualize the observed spectra. The observed transmittances above 122 km are almost unity, because the solar light is not yet being absorbed by the atmosphere. At altitudes lower than 122 km, the standard deviation on the observed transmittance is small enough to isolate an individual observed transmittance

(Vandaele et al. 2008, 2013) (ex. Fig. 2). The tangent altitude of each measurement is defined as the minimum distance between the surface of Venus and the instrument line of sight. As Vex/SOIR moved along its orbit, successive tangent altitudes were defined. SOIR acquired observations either at sunset or at sunrise on a 1-s time cycle. The instrument probed the Venus atmosphere at the terminator, which is a unique region, since it represents the boundary between the dark and illuminated sides of the planet. The local solar time of each observation was always 6 AM or 6 PM, because the evening occultation occurred when the Sun was setting (as seen from SOIR) and the morning occultation occurred when the Sun was rising.

SOIR transmittance

At the beginning of an occultation, the solar light path does not traverse the Venus atmosphere. SOIR starts recording solar spectra at the outer region of the atmosphere to obtain at least 40 spectra and to define the reference Sun spectra. For tangent altitudes lower than 220 km, the observed transmittances are calculated by dividing the spectrum recorded at the current time by the reference Sun spectrum. At lower altitudes, the instrument line of sight penetrates deeper into the atmosphere, and continuum absorption—over an order width—occurs due to haze and atmospheric molecules such as CO_2. At the end of an occultation, the signal becomes zero, because the solar light is completely absorbed by the clouds and atmospheric species.

Figure 2 gives an example of the observed transmittances during one occultation (orbit 591.1, Dec. 3, 2007, order 147, latitude 9°S, longitude 209°). As shown in Fig. 2, the observed transmittances above 122 km are almost unity within the noise, because the solar light is not yet absorbed by the atmosphere. On the other hand, the difference between the spectra recorded at 121.02 km and 115.54 km is 0.33%, while the standard deviation at such altitudes is on the order of 0.04%. The standard deviation of an observed transmittance is calculated as:

$$S = \sqrt{\frac{1}{n}\sum_{i=1}^{n}(x_i - \bar{x})^2}, \quad (1)$$

where n is the number of spectra at a particular altitude, x_i represents the observed values, and $\bar{x}$ is the mean value of the observations at that altitude. Additionally, systematic errors, such as those due to pointing errors, may be canceled out when the spectral ratio is calculated, because an occultation is basically a relative measurement. The methods used to estimate the pointing drift and detector sensitivity drift are described in "Appendix".

It is found that the standard deviation of the observed transmittance is small enough to isolate an individual observed transmittance regardless of the high altitudes (above 90 km) of the observations. In this work, we will work with spectra obtained at altitudes between 70 and 120 km; the effect of molecular spectral absorption has been removed from these spectra (see "Removal of the molecular absorption effect" section for details on this procedure).

Figure 3 and Table 1 show the latitudinal distribution of all the observations considered in this work. These observations are also listed in Table 2 (morning occultations) and Table 3 (evening occultations). The orders that have no strong CO_2 absorption bands are considered, whereas the orders covering the CO_2 band at 3 μm (orders 152 to 169) and 3.7 μm (orders 101 to 110) are not considered.

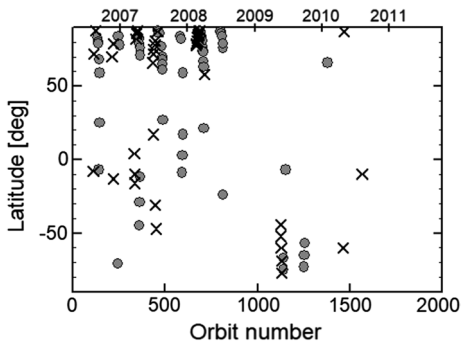

Fig. 3 The latitudes of selected SOIR occultations are plotted as a function of the VEX orbit number. The corresponding first days of each Earth year are given at the top of the figure. The dots (●) are for morning solar occultations, while the crosses (×) are for evening solar occultations. There is one orbit per Earth day. There are 128 occultations considered in this work. The data cover the period from 2006 to 2010

Table 1 Latitudinal distribution of the occultations assuming hemispheric symmetry

Latitude bin	Morning occultations	Evening occultations
High lat. (60°–90°, Eq. symmetry)	56	32
Low lat. (0°–60°, Eq. symmetry)	21	15

Method of analysis

Removal of the molecular absorption effect

The gas transmittance T_{gas} due to atmospheric molecules such as CO_2, H_2O, HCl, and HF, which have absorption lines in the orders considered in this work, is removed from the observed transmittance T_{obs}. T_{gas} is calculated as:

$$T_{gas} = e^{-\tau_{gas}}, \quad (2)$$

where τ_{gas} is the total optical thickness due to all species obtained as:

$$\tau_{gas} = \sum_i \tau_i, \quad (3)$$

where τ_i is the optical thickness of species i (i=CO_2, H_2O, HCl, and HF), integrated along the full line of sight (LOS):

$$\tau_i = \sigma_i \int_{LOS} n_i \, ds, \quad (4)$$

where σ_i and n_i are the absorption cross section and the number density of species i, respectively. The absorption cross sections are calculated using a line-by-line method taking the CO_2 parameters from the HITEMP database (Wattson and Rothman 1992) and the other parameters from the HITRAN 2012 databases (Rothman et al. 2013). The initial number densities and temperature and pressure profiles are taken from the Venus International Reference Atmosphere (VIRA) model (Seiff et al. 1985). Only the absorption lines present in the central order are considered in the calculation of the synthetic spectra. As an approximation, we do not consider the diffraction

Table 2 Morning occultations employed in this study

Central wavenumber (cm^{-1})	Orbit	Day [dd/mm/yyyy]	Lat. [deg]	Lon. [deg]	Central wavenumber (cm^{-1})	Orbit	Day [dd/mm/yyyy]	Lat. [deg]	Lon. [deg]
2738.18	133	1/9/2006	83	218	3344.18	366	22/4/2007	71	228
2738.18	145	13/9/2006	25	273	3344.18	465	30/7/2007	87	231
2738.18	145.2	13/9/2006	59	270	3344.18	467	1/8/2007	86	224
2760.63	133	1/9/2006	83	218	3344.18	479	13/8/2007	77	235
2760.63	145	13/9/2006	25	273	3344.18	484	18/8/2007	70	246
2760.63	145.2	13/9/2006	59	270	3344.18	485	19/8/2007	68	249
2917.74	143	11/9/2006	68	262	3344.18	486	20/8/2007	65	251
2917.74	242	19/12/2006	−71	207	3344.18	487	21/8/2007	61	253
2917.74	356	12/4/2007	84	183	3344.18	487.2	21/8/2007	27	250
2917.74	357	13/4/2007	83	189	3344.18	583	25/11/2007	84	163
2917.74	693	14/3/2008	85	194	3344.18	586	28/11/2007	82	177
2917.74	801	30/6/2008	87	86	3344.18	591	3/12/2007	−9	209
2917.74	803	2/7/2008	86	108	3344.18	593	5/12/2007	3	215
2917.74	807	6/7/2008	84	135	3344.18	595	7/12/2007	17	220
2917.74	812	11/7/2008	79	158	3344.18	687	8/3/2008	88	223
2917.74	813	12/7/2008	−24	175	3344.18	688	9/3/2008	87	213
2917.74	815	14/7/2008	76	170	3344.18	689	10/3/2008	87	205
3276.85	137	5/9/2006	79	237	3344.18	690	11/3/2008	87	200
3276.85	141	9/9/2006	−7	262	3344.18	691	12/3/2008	86	197
3299.29	136	4/9/2006	80	233	3344.18	693	14/3/2008	85	194
3299.29	137	5/9/2006	79	237	3344.18	695	16/3/2008	84	194
3299.29	141	9/9/2006	−7	262	3344.18	697	18/3/2008	82	196
3299.29	361	17/4/2007	79	208	3344.18	699	20/3/2008	81	198
3299.29	591	3/12/2007	−9	209	3344.18	703	24/3/2008	77	206
3299.29	593	5/12/2007	3	215	3344.18	705	26/3/2008	74	210
3321.73	137	5/9/2006	79	237	3344.18	706	27/3/2008	73	212
3321.73	255	1/1/2007	78	267	3344.18	709	30/3/2008	67	219
3344.18	137	5/9/2006	79	237	3344.18	710.1	31/3/2008	63	221
3344.18	141	9/9/2006	−7	262	3344.18	710.2	31/3/2008	21	217
3344.18	247	24/12/2006	84	255	3344.18	1139	3/6/2009	−75	91
3344.18	356	12/4/2007	84	183	3344.18	1141	5/6/2009	−67	100
3344.18	357	13/4/2007	83	189	3344.18	1154	18/6/2009	−7	144
3344.18	358	14/4/2007	82	194	3344.18	1252	24/9/2009	−73	95
3344.18	359	15/4/2007	−45	216	3344.18	1254	26/9/2009	−65	98
3344.18	462	27/7/2007	88	255	3344.18	1256	28/9/2009	−57	103
3344.18	361	17/4/2007	79	208	3344.18	1381	31/1/2010	66	131
3344.18	362	18/4/2007	−29	224	3972.61	812	11/7/2008	79	158
3344.18	363	19/4/2007	76	216	3995.06	699	20/3/2008	81	198
3344.18	365	21/4/2007	−12	233					

order addition procedure, because the AOTF bandpass function is wider than the spectral width of the detector, implying that more than one diffraction order is measured by the detector (Mahieux et al. 2012). This approximation is valid here, since the value of the AOTF transfer function is negligible in the adjacent orders when compared to the central order since we considered only the main orders, for which the absorption structures in the adjacent orders are weak [see Mahieux et al. 2015a (the paper about the rotational temperature)]. T_{gas} is fitted by adjusting the number density of the gas species and convolving the absorption cross section by a triangular filter ($0.14 cm^{-1}$ FWHM). An example of T_{gas} and T_{obs} is given in Fig. 4 for a typical observation (Sep. 05, 2006,

Table 3 Evening occultations employed in this study

Central wavenumber (cm^{-1})	Orbit	Day [dd/mm/yyyy]	Lat. [deg]	Lon. [deg]	Central wavenumber (cm^{-1})	Orbit	Day [dd/mm/yyyy]	Lat. [deg]	Lon. [deg]
2738.18	110	9/8/2006	−8	344	3344.18	442	7/7/2007	78	285
2738.18	111	10/8/2006	72	351	3344.18	445	10/7/2007	81	292
2738.18	217	24/11/2006	−13	317	3344.18	458	11/7/2007	87	293
2738.18	219	26/11/2006	79	317	3344.18	667	15/7/2007	78	259
2760.63	110	9/8/2006	−8	344	3344.18	669	19/2/2008	79	263
2760.63	111	10/8/2006	72	351	3344.18	671	21/2/2008	81	268
2760.63	217	24/11/2006	−13	317	3344.18	674	24/2/2008	83	273
2760.63	219	26/11/2006	79	317	3344.18	675	25/2/2008	83	275
2917.74	124	23/8/2006	88	88	3344.18	677	27/2/2008	84	277
2917.74	211	18/11/2006	70	296	3344.18	679	29/2/2008	85	277
2917.74	341	28/3/2007	82	348	3344.18	681	2/3/2008	86	274
2917.74	433	28/6/2007	66	262	3344.18	684	5/3/2008	88	257
2917.74	445	10/7/2007	81	292	3344.18	685	6/3/2008	88	247
3299.29	335	22/3/2007	−16	319	3344.18	686	7/3/2008	88	235
3344.18	332	19/3/2007	4	310	3344.18	711.1	1/4/2008	58	223
3344.18	334	21/3/2007	−10	316	3344.18	1124	19/5/2009	−44	234
3344.18	335	22/3/2007	−16	319	3344.18	1126	21/5/2009	−52	240
3344.18	341	28/3/2007	82	348	3344.18	1128	23/5/2009	−60	247
3344.18	345	1/4/2007	86	13	3344.18	1130	25/5/2009	−69	255
3344.18	347	3/4/2007	87	36	3344.18	1132	27/5/2009	−77	264
3344.18	349	5/4/2007	88	80	3344.18	1465	25/4/2010	−60	200
3344.18	436.1	1/7/2007	72	270	3344.18	1467	27/4/2010	87	242
3344.18	436.2	1/7/2007	17	272	3344.18	1567	5/8/2010	−10	159
3344.18	438	3/7/2007	75	275					

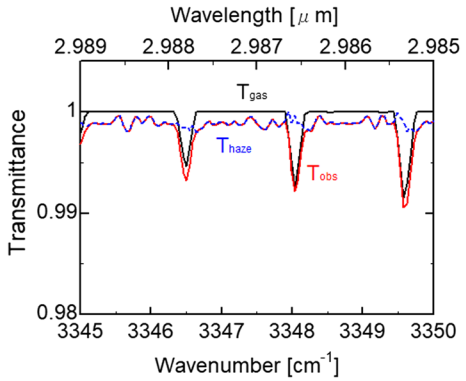

Fig. 4 Example of a calculated transmittance (T_{gas}, black spectrum), an observed transmittance (T_{obs}, red spectrum), and a residual transmittance (T_{haze}, dotted blue spectrum) measured at an altitude of 110.3 km corresponding to the observation obtained on Sep. 05, 2006 (order 149, orbit 137.1, latitude 79 N°, longitude 237°). These wavelengths are selected to visualize the analysis method

order 149, orbit 137, latitude 79 N°, longitude 237°, altitude 110.3 km). T_{haze} is obtained by dividing T_{obs} by T_{gas} at each observed altitude as:

$$T_{haze} = \frac{T_{obs}}{T_{gas}} \tag{5}$$

Retrieval of the haze optical properties

Each solar occultation measurement can be assigned to a specific altitude at the limb. As shown in Fig. 1, the tangent altitude h_{tg} decreases with time during the occultation in the case of an ingress. The tangent altitude $h_{tg,j}$ corresponding to the jth measurement defines an atmospheric shell. The region between two successive measurement altitudes $h_{tg,j-1}$ and $h_{tg,j}$ defines the jth layer (L_j).

τ_j, the horizontal optical thickness corresponding to layer L_j and all the above-located layers, is defined as:

$$\tau_j = -\ln\left(T_{haze,j}\right), \tag{6}$$

where $T_{haze,j}$ is defined in Eq. (5) for the jth observation path.

$\tau_{j,in}$, the horizontal optical thickness of layer L_j, is obtained considering the so-called onion peeling method and can be written as:

$$\tau_{j,in} = \tau_j - \sum_{i=1}^{j-1} 2\,dx_i \times k_i, \tag{7}$$

where k_i is the aerosol extinction coefficient of layer L_i and dx_i is the horizontal path length in layer L_i, which is outside relative to layer L_j.

We define the local extinction coefficient k_j, calculated by dividing $\tau_{j,in}$ by the local length $2\,\mathrm{d}x_j$, as:

$$k_j = \frac{\tau_{j,in}}{2\,\mathrm{d}x_j}, \tag{8}$$

where the factor 2 comes from the symmetry on both sides of the tangent point.

The vertical distribution of extinction coefficients is obtained by repeating the process described above. Figure 5 (top) is an example of the vertical distribution of the extinction coefficient. The extinction error Δk is estimated as:

$$\Delta\tau_j = \frac{\Delta T_{\mathrm{haze},j}}{T_{\mathrm{haze},j}} \tag{9}$$

$$\Delta\tau_{j,in} = \sqrt{\left(\Delta\tau_j\right)^2 + \left(\sum_{i=1}^{j-1}(2\mathrm{d}x_i \times \Delta k_i)\right)^2} \tag{10}$$

$$\Delta k_j = \frac{\Delta\tau_{j,in}}{2\mathrm{d}x_j}, \tag{11}$$

where $\Delta T_{\mathrm{haze},j}$ is the standard deviation of $T_{\mathrm{haze},j}$, calculated using Eq. (1), and $\Delta T_{\mathrm{haze},j}$ is estimated to be 0.1%, whereas the average Δk_j for all observations is estimated to be almost 30% at all observation paths. Δk_j becomes much larger than $\Delta T_{\mathrm{haze},j}$ because of the errors accumulated layer by layer through the sum in Eq. (10).

The vertical optical thickness τ_{vert} is calculated by integrating the extinction vertically as:

$$\tau_{\mathrm{vert}} = \int k_j \mathrm{d}z. \tag{12}$$

The normalized extinction m_j (in dimensions of the mixing ratio) is defined as:

$$m_j = \frac{k_j}{n_{\mathrm{CO}_2} \cdot S}, \tag{13}$$

where n_{co_2} is the total CO_2 number density in layer L_j and S is the extinction coefficient cross section. The normalized extinction coefficient is a nondimensional quantity. The total CO_2 number density is obtained from previous studies (Mahieux et al. 2010, 2012, 2015a). S is the CO_2 Rayleigh scattering cross section at 3.0 μm, which is expected to be equal to $1.1 \times 10^{-29}\,[\mathrm{cm}^2]$, extrapolated from the values in the visible region (in Table 8-2 of Tohmatsu and Ogawa 1990). Figure 5 (bottom) is an example of the vertical distribution of the normalized extinction coefficient. The errors of τ_{vert} and m_j are estimated as:

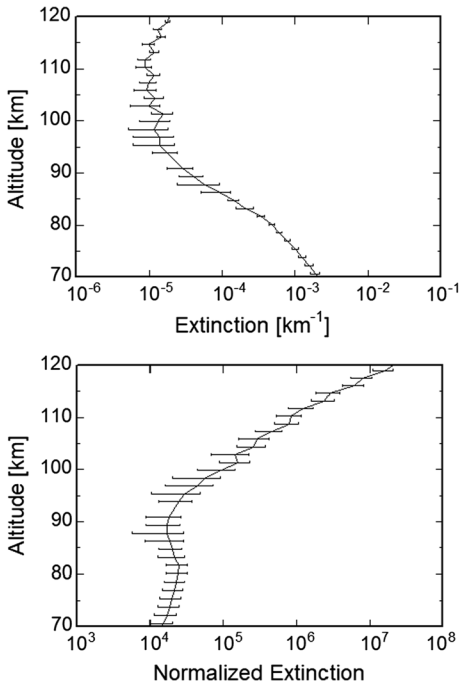

Fig. 5 Example of a vertical profile of extinction coefficients (top panel) and the corresponding normalized extinction coefficients (bottom panel) for orbit 137, order 149 (Sep. 05, 2006, latitude 79 N°, longitude 237°). The average errors are almost 26% for the extinction coefficient and 42% for the normalized extinction coefficient

$$\Delta\tau_{\mathrm{vert}} = \sum_{i=1}^{j}(\Delta k_i \times \mathrm{d}z) \tag{14}$$

$$\Delta m_j = \sqrt{\left(\frac{\Delta k_j}{n_{\mathrm{co}_2} \cdot S}\right)^2 + \left(\frac{k_j \cdot \Delta n_{\mathrm{co}_2}}{(n_{\mathrm{co}_2})^2 \cdot S}\right)^2}, \tag{15}$$

where Δn_{CO_2} is the error on the CO_2 number density, which was obtained from previous studies (Mahieux et al. 2010, 2012, 2015a). The average Δm for all observations is estimated to be 40% for all observations.

Results

Extinction profiles

The average extinction coefficient profiles are plotted in Fig. 6 (for the morning and evening sides of the terminator and for high and low latitudes). As shown in these profiles, we observe that hazes also appear to be present at altitudes above 90 km. Moreover, the extinction coefficient profiles show an obvious change in the slope at ∼ 95km. Finally, the extinction coefficients at low latitudes are larger than those at high latitudes, and this ratio is smaller than that already reported by Wilquet et al. (2012). In the 70–90 km altitude region, the average vertical optical thickness is equal to 0.19

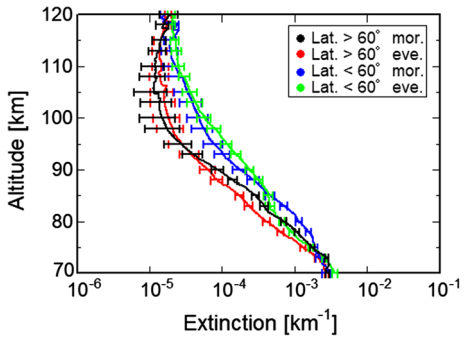

Fig. 6 Average extinction coefficient profiles for morning high-latitude (latitude > 60°, black line), evening high-latitude (latitude > 60°, red line), morning low-latitude (latitude < 60°, blue line), and evening low-latitude (latitude < 60°, green line) observations. The average of the variability is 21.5% for the morning high-latitude observations

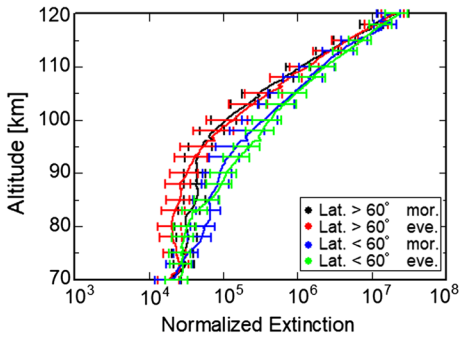

Fig. 7 Average of all normalized extinction coefficients for morning high-latitude (latitude > 60°, black line), evening high-latitude (latitude > 60°, red line), morning low-latitude (latitude < 60°, blue line), and evening low-latitude (latitude < 60°, green line) observations. The average of the variability is 34.3% for the morning high-latitude observations

and 0.24 for the high- and low-latitude regions, respectively. In the 90–110 km altitude region, the average vertical optical thickness is equal to 0.005 and 0.015 for the high- and low-latitude regions, respectively. The mean variability for all the observations is 12% for the 70–90 km region and 14% for the 90–110 km region. The optical thickness at low latitudes is larger than that at high latitudes. However, Kawabata et al. (1980) showed that the haze optical thickness is larger at high latitudes than at low latitudes. Braak et al. (2002) reported a long-term temporal variation in the haze optical thickness, which decreased by a factor of 0.3 between 1980 and 1992. The high-latitude optical thickness was relatively large in the recent past.

Normalized extinction coefficients

The average normalized extinction coefficient profiles are plotted in Fig. 7 (for the morning and evening sides and for high and low latitudes). A significant increase in the normalized extinction coefficient with the altitude is observed above 90 km for both the high- and the low-latitude regions. The normalized extinction coefficients for both the morning and the evening occultations at low latitudes are almost one order of magnitude larger than those at high latitudes at altitudes above 90 km.

Discussion

In Esposito et al. (1983), the upper haze layer was observed at altitudes as high as 90 km. Additionally, the presence of high-altitude haze was inferred from VMC images and from SPICAV-IR and UV occultations onboard Venus Express (Limaye et al. 2015; Luginin et al. 2016). We derived the haze optical properties at altitudes above 90 km with SOIR data. We showed that haze is present at such high altitudes and that the normalized extinction coefficient increases above 90 km at both high and low latitudes. The relationship between sulfur compounds and haze has already been discussed by several previous studies (Mills et al. 2007; Zhang et al. 2012). Recently, observations of SO and SO_2 at high altitudes have been reported; for example, SOIR detected an increase in the SO_2 VMR above 85 km at the terminator (Mahieux et al. 2015b). Belyaev et al. (2012) reported the presence of two layers of SO and SO_2: a lower layer between 65 and 80 km observed by SOIR and an upper layer between 85 and 105 km observed by the UV channel of the SPICAV/SOIR instrument. The mixing ratios of SO and SO_2 decrease from 0.2 to 0.02 ppmv between 65 and 80 km and increase from 0.05 to 2 ppmv between 85 and 105 km. We postulate that the increases in the SO and SO_2 mixing ratios between 85 and 105 km and the increase in the haze extinction coefficient between these altitudes may be either coincidental or connected. Such a connection does not seem likely between 65 and 80 km. However, it is still unclear how haze is produced and of what its composition consists. We speculate that sources of SO and SO_2, such as H_2SO_4 or Sx, are transported upwards and are then photodissociated.

The following process is proposed to explain the observed increase in the haze normalized extinction coefficient at high altitudes (above 90 km):

(1) Sources of haze particles (such as H_2SO_4 or S_X) are transported upward at a velocity larger than the sedimentation velocity from the cloud deck.
(2) These transported aerosols either evaporate (in the case of H_2SO_4, see Zhang et al. (2012), for example)

or react with other compounds (sulfur and oxygen atoms), and SO and SO_2 will be produced at high altitudes. For example, Mills and Allen (2007) and Zhang et al. (2012) proposed detailed formation schemes starting either from H_2SO_4 or S_X to form SO and SO_2.

(3) Haze can be produced by chemical processes at such high altitudes through a series of chemical reactions initiated in particular by the photodissociation of SO and SO_2, as discussed in Mills and Allen (2007) and Zhang et al. (2012).

(4) The size of the produced haze particles should be smaller than those of particles transported from their sources for the following reason.

The extinction coefficient is defined as:

$$k = \sigma \cdot N, \tag{16}$$

where σ is the extinction cross section and N is the number density of the scattering material. When the haze particles become smaller, keeping the haze mass constant, the extinction cross sections decrease, and the number density becomes larger. For example, when the particle size is divided by two, the extinction cross section becomes four times smaller; on the other hand, the number density becomes eight times larger. Under these circumstances, the extinction coefficient becomes larger when the particles are produced by chemical reactions than when the sources of haze are transported from below.

The normalized extinction coefficients can increase at high altitudes because of the processes proposed above. Figure 7 shows that the normalized extinction coefficients at low latitudes are almost one order of magnitude larger than those at high latitudes. This can be explained by the fact that haze is produced in a larger amount at low latitudes than at high latitudes. From the previous discussion, larger aerosols are likely transported to these higher altitudes, while smaller particles are produced there. This explanation could be verified by numerical models. This hypothesis is compatible with the measurements of Wilquet et al. (2009), who demonstrated the existence of at least two types of particles at high altitudes: mode 1 of mean radius $0.1 \leqq r \leqq 0.3$ μm and mode 2 of $0.4 \leqq r \leqq 1.0$ μm.

Conclusions

The optical properties of the upper haze layer at altitudes above 90 km were studied in this work. A significant increase in the normalized extinction coefficient was also observed above 90 km at both high and low latitudes, which could be linked to the vertical profiles of SO and SO_2. The processes by which the normalized extinction coefficient increases were discussed, and we proposed the following mechanisms to explain our observations. Aerosols, including sulfur-based compounds, are transported upwards at a velocity larger than the sedimentation velocity from the cloud deck. The transported aerosols then evaporate or react to produce SO and SO_2 at such high altitudes. At high altitudes, haze particles are produced by chemical processes involving SO and SO_2. Since the normalized extinction coefficient increases at high altitudes, we propose that the size of the haze particles that are produced is smaller than those of transported aerosol particles. Haze seems to be produced in a larger extent at low latitudes than at high latitudes, as deduced from the normalized extinction coefficients that are several times larger at low latitudes than at high latitudes.

Acknowledgements

Venus Express is a planetary mission operated by the European Space Agency (ESA). We wish to thank all ESA members who participated in the mission, particularly H. Svedhem and D. Titov. We thank our collaborators at IASB-BIRA (Belgium), LATMOS (France), and IKI (Russia). We thank CNES, CNRS, Roskosmos, and the Russian Academy of Science. This research program was supported by the Belgian Federal Science Policy Office and the European Space Agency (ESA, PRODEX program, contracts C 90268, 90113, and 17645). A. Mahieux thanks the FNRS for the position of "chargé de recherches". We acknowledge the support of the "Interuniversity Attraction Poles" program financed by the Belgian government (Planet TOPERS). The research leading to these results has received funding from the European Union Seventh Framework Program (FP7/2007-2013) under grant agreement n°606798 (EuroVenus). N.I. acknowledges partial support from JSPS KAKENHI grant JP16H02225.

Authors' contributions

ST analyzed and interpreted the observation data regarding the upper haze layer above Venus and was the major contributor in writing the manuscript. NI contributed to improving the logic and discussion of the manuscript. MA wrote "Description of the observations" section about the instrumentation. All authors read and approved the final manuscript.

Funding

There are no sources of funding to report.

Availability of data and materials

The data sets used and analyzed during the current study are available from the corresponding author on reasonable request.

Competing interests

The authors declare that they have no competing interests.

Author details

[1] Department of Earth and Planetary Sciences, Hokkaido University, Faculty of Science, Kita 10, Nishi 8, Kita-ku, Sapporo 060-0810, Japan. [2] Belgian Institute for Space Aeronomy, 3 Av. Circulaire, B-1180 Brussels, Belgium. [3] Fonds National de la Recherche Scientifique, Brussels, Belgium. [4] 4-18-9 Akatutumi Setagaya-ku, Tokyo 156-0044, Japan.

Appendix

Figure 8 (Vandaele et al. 2013) and Fig. 9 (Trompet et al. 2016) show examples of the signal obtained during one solar occultation. These examples correspond to an egress (Fig. 8) when the tangent altitude increases with time (sunrise), and an ingress (Fig. 9) when the tangent altitude decreases with time (sunset). The top panels

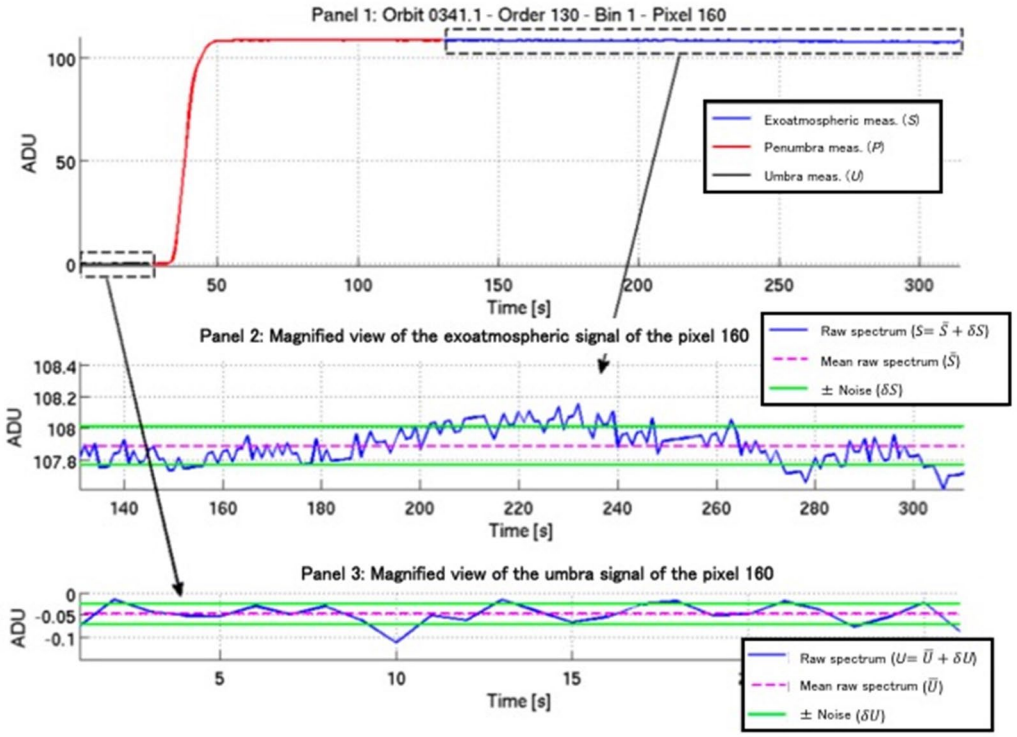

Fig. 8 Panel 1: Typical evolution through time of the signal (in ADU) on one pixel of the detector during a solar occultation. This example corresponds to an egress: at the beginning, no light reaches the detector when VEX is in the umbra region (black line); then, the occultation occurs when VEX is in the penumbra region (red line); finally, the instrument looks directly at the Sun and measures exoatmospheric raw spectra (blue line). The exoatmosphere and umbra zones used to derive the noise are indicated by the boxes. Panels 2 and 3: Variation of the noise signal around the mean value of the two zones (exoatmosphere in Panel 2 and umbra region in Panel 3). The standard deviations are shown by the lines in green (taken from A.C. Vandaele et al. 2013)

of Figs. 8 and 9 show the signal in analog digital units (ADU) measured on one detector pixel during a solar occultation. In the case of Fig. 8, the signal can be separated into three parts: at the beginning, no light reaches the SOIR when Venus Express is in the umbra region (black line); then, the occultation occurs when Venus Express is in the penumbra region (red line); finally, the instrument looks directly at the Sun and measures exoatmospheric raw spectra without atmospheric absorption (blue line). The middle panel of Fig. 8 and the bottom panel of Fig. 9 show the process of determining the signal level in the exoatmosphere. There are significant changes at 30–50 s (Fig. 8) and at 260–280 s (Fig. 9). In these cases, the whole exoatmospheric level is determined with the regression lines for tangent altitudes of 220 km or above (after 130 s in Fig. 8, before 180 s in Fig. 9).

Fluctuations in the level due to pointing drift are shown in the middle panel of Fig. 8 and in the enlarged figure in the bottom panel of Fig. 9; in these cases, the raw spectrum are ± 0.1 ADU/108 ADU $= \pm 0.09\%$ and ± 0.05 ADU/20 ADU $= \pm 0.25\%$, respectively. These values are on the same level or less than the difference between the spectra recorded at 121.02 km and 115.54 km (0.33%, Fig. 2 in this work). That is, observed transmittances up to 120 km are significant even if pointing drift is considered.

Fluctuations in the level due to detector sensitivity drift are not found in Fig. 8 (less than 0.1% per 100 s), but are found in Fig. 9 as an inclination of the regression line. The inclination is estimated to be approximately 1% per 100 s in the exoatmosphere and 0.2% per 20 s mainly during observations (260–280 s). These values are on the same level or less than the difference between the spectra recorded at 121.02 km and 115.54 km (0.33%, Fig. 2 in this work). That is, observed transmittances up to 120 km are significant even if detector sensitivity drift is considered. However, other potential sources (e.g., pointing drift) may be included in this study. The above explanation does not evaluate the measurement errors due to pointing drift and detector sensitivity drift directly. However, this estimation of measurement errors should be effective.

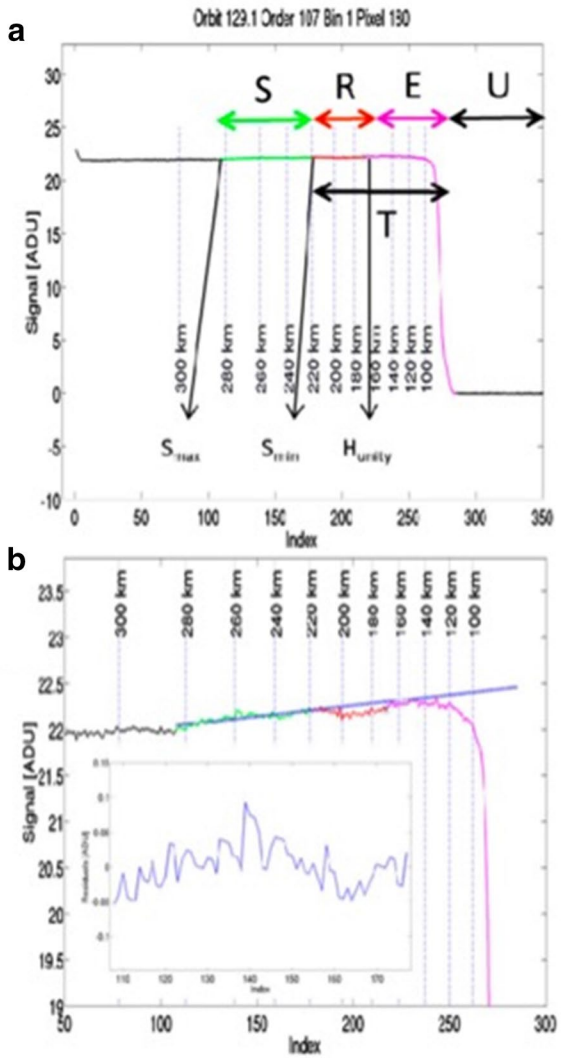

Fig. 9 (A) Separation of the Sun region into different zones for one detector pixel as a function of the index, i.e., the time after the beginning of the measurement. Lines corresponding to specific tangent altitudes are plotted. (B) Plot of the fit over the S region and extrapolation in the T region. The graph inside shows the residuals of the fit (taken from Trompet et al. 2016)

Received: 20 March 2019 Accepted: 1 November 2019
Published online: 21 November 2019

References

Belyaev D, Korablev O, Frdorova A, Bertaux J-L, Vandaele A-C, Montmessin F, Mahieux A, Wilquet V, Drummond R (2008) First observations of SO_2 above Venus' clouds by means of Solar Occultation in the InfraRed. J Geophys Res 113:E00B25

Belyaev D, Montmessin F, Bertaux J-L, Mahieux A, Frdorova A, Korablev O, Marcq E, Yung Y, Zhang Z (2012) Vertical profiling of SO_2 and SO above Venus' clouds by SPICAV/SOIR solar occultations. Icarus 217:740–751

Bertaux J-L, Vandaele A-C, Korablev O, Villard E, Fedorova A, Fussen D, Quemerais E, Belyaev D, Mahieux A, Montmessin F, Muller C, Neefs E, Nevejans D, Wilquet V, Dubois JP, Hauchecorne A, Stepanov A, Vinogradov I, Rodin A, SPICAV/SOIR team (2007) A warm layer in Venus' cryosphere and high-altitude measurements of HF, HCl, H_2O and HDO. Nature 450:646–649

Braak CJ, Haan JF, Hovenier JW (2002) Spatial and temporal variations of Venus haze properties obtained from Pioneer Venus Orbiter polarimetry. J Geophys Res 107(E5):5029

de Kok R, Irwin PGJ, Tsang CCC, Piccioni G, Drossart P (2011) Scattering particles in nightside limb observations of Venus' upper atmosphere by Venus Express VIRTIS. Icarus 211(1):51–57

Esposito LW (1984) Sulfur dioxide: episodic injection shows evidence for active Venus Volcanism. Science 223:1072–1074

Esposito LW, Knollenberg RG, Marov MYa, Toon OB, Turco RP (1983) The Clouds and hazes of Venus. In: Hunten DM, Colin L, Donahue TM, Moroz VI (eds) Venus. University of Arizona Press, Tucson, pp 484–564

Esposito LW, Copley M, Eckert R, Gates L, Stewart AIF, Worden H (1988) Sulfur dioxide at the Venus cloud tops, 1978–1986. J Geophys Res 93(D5):5267

Hansen JE, Hovenier JW (1974) Interpretation of the polarization of Venus. J Atmos Sci 31:1137–1160

Kawabata K, Coffeen DL, Hansen JE, Lane WA, Sato M, Travis LD (1980) Cloud and haze properties from Pioneer Venus polarimetry. J Geophys Res 85:8129–8140

Limaye SS, Markiewicz WJ, Krauss R, Ignatiev N, Roatsch T, Matz KD (2015) Focal lengths of Venus monitoring camera from limb locations. Planet Space Sci 113–114:169–183

Luginin M, Fedorova A, Belyaev D, Montmessin F, Wilquet V, Korablev O, Bertaux J-L, Vandaele AC (2016) Aerosol properties in the upper haze of Venus SPICAV IR data. Icarus 277:154–170

Mahieux A, Berkenbosch S, Clairquin R, Fussen D, Mateshvili N, Neefs E, Nevejans D, Ristic B, Vandaele AC, Wilquet V, Belyaev D, Fedorova A, Korablev O, Villard E, Montmessin F, Bertaux J-L (2008) In-flight performance and calibration of SPICAV SOIR onboard Venus Express. Appl Opt 47:2252–2265

Mahieux A, Wilquet V, Drummond R, Belyaev D, Fedorova A, Vandaele AC (2009) A New Method for Determining the transfer function of an Acousto Optical Tunable Filter. Opt Express 17:2005–2014

Mahieux A, Vandaele AC, Neefs E, Robert S, Wilquet V, Drummond R, Fedorova A, Bertaux JL (2010) Densities and temperatures in the Venus mesosphere and lower thermosphere retrieved from SOIR on board Venus Express: retrieval technique. J Geophys Res 115:E12014

Mahieux A, Vandaele AC, Robert S, Wilquet V, Drummond R, Montmessin F, Bertaux J-L (2012) Densities and temperatures in the Venus mesosphere and lower thermosphere retrieved from SOIR on board Venus Express: carbon dioxide measurements at Venus terminator. J Geophys Res 117:E07001

Mahieux A, Vandaele AC, Bougher SW, Drummond R, Robert S, Wilquet V, Chamberlain S, Piccialli A, Montmessin F, Tellmann S, Pätzold M, Häusler B, Bertaux JL (2015a) Update of the Venus density and temperature profiles at high altitude measured by SOIR on board Venus Express. Planet Space Sci 113–114:309–320

Mahieux A, Vandaele AC, Robert S, Wilquet V, Drummond R, Chamberlain S, Belyaev D, Bertaux JL (2015b) Venus mesospheric sulfur dioxide measurement retrieved from SOIR on board Venus Express. Planet Space Sci 113–114:193–204

Mills FP, Allen M (2007) A review of selected issues concerning the chemistry in Venus' middle atmosphere. Planet Space Sci 55:1729–1740

Mills FP, Esposito LW, Yung YL (2007) Atmospheric composition, chemistry, and clouds. In: Esposito LW, Stofan E, Cravens T (eds) Exploring Venus as a terrestrial planet. American Geophysical Union, Washington, D.C

Nevejans D, Neefs E, Ransbeeck EV, Berkenbosch S, Clairquin R, Vos LD, Moelans W, Glorieyx S, Baeke A, Korablev O, Vinogradov I, Kalinnikov Y, Bach B, Dubois JP, Villard E (2006) Compact high-resolution spaceborne echelle grating spectrometer with acousto-optical tunable filter based order sorting for the infrared domain from 2.2 to 4.3 µm. Appl Opt 45:5191–5206

Rothman LS, Gordon IE, Babikov Y, Barbe A, Chris Benner D, Bernath PF, Birk M, Bizzocchi L, Boudon V, Brown LR, Campargue A, Chance K, Cohen EA, Coudert LH, Devi VM, Drouin BJ, Fayt A, Flaud J-M, Gamache RR, Harrison JJ, Hartmann J-M, Hill C, Hodges JT, Jacquemart D, Jolly A, Lamouroux J, Le Roy RJ, Li G, Long DA, Lyulin OM, Mackie CJ, Massie ST, Mikhailenko S, Müller HSP, Naumenko OV, Nikitin AV, Orphal J, Perevalov V, Perrin A, Polovtseva ER, Richard C, Smith MAH, Starikova E, Sung K, Tashkun S, Tennyson J, Toon GC, VI G, Tyuterev G Wagner (2013) The HITRAN 2012

molecular spectroscopic database. J Quant Spectrosc Radiat Transfer 130:4–50
Sandor BJ, Clancy RT, Schieven GM (2012) Upper limits for H_2SO_4 in the mesosphere of Venus. Icarus 217:839–844
Sato M, Travis LD, Kawabata K (1996) Photopolarimetry analysis of the Venus atmosphere in polar regions. Icarus 124:569–585
Seiff A, Schofield JT, Kliore AJ, Taylor FW, Limaye SS, Revercomb HE, Sromovsky LA, Kerzhanovich VV, Moroz VI, Marov M Ya (1985) Models Of the structure of the atmosphere of Venus from the surface to 100 kilometers altitude. Adv Space Res 5(11):3–58
Svedhem H, Titov D, McCoy D, Lebreton J-P, Barabash S, Bertaux JL, Drossart P, Formisano V, Häusler B, Korablev O, Markiewicz WJ, Nevejans D, Pätzold M, Piccioni G, Zhang TL, Taylor FW, Lellouch E, Koschny D, Witasse O, Eggel H, Warhaut M, Accomazzo A, Rodriguez-Canabal J, Fabrega J, Shirmann T, Clochet A, Coradini M (2007) Venus express: the first European mission to Venus. Planet Space Sci 55:1636–1652
Takagi S, Iwagami N (2011) Contrast sources for the infrared images taken by the Venus mission AKATSUKI. Earth Planets Space 63:435–442. https://doi.org/10.5047/eps.2011.01.007
Tohmatsu T, Ogawa T (1990) Compendium of Aeronomy. Terra Scientific Publishing Company, Tokyo
Trompet L, Mahieux A, Ristic B, Robert S, Wilquet V, Thomas IR, Vandaele AC (2016) Improved algorithm for the transmittance estimation of spectra obtained with SOIR/Venus Express. Appl Opt 55:9275–9281
Vandaele AC, De Maziere M, Drummond R, Mahieux A, Neefs E, Wilquet V, Korablev O, Fedorova A, Belyaev D, Montmessin F, Bertaux J-L (2008) Comparison of the Venus mesosphere measured by Solar Occultation at Infrared on board Venus Express. J Geophys Res 113:E00B23
Vandaele AC, Mahieux A, Robert S, Berkenbosch S, Clairquin R, Drummond R, Letocart V, Neefs E, Ristic B, Wilquet V, Colomer F, Belyaev D, Bertaux JL (2013) Improved calibration of SOIR/Venus express spectra. Opt Express 21:21148
Wattson RB, Rothman LS (1992) Direct numerical diagonalization: wave of the future. J Quant Spectrosc Radiat Transfer 48:763–780
Wilquet V, Fedorova A, Montmessin F, Drummond R, Mahieux A, Vandaele AC, Villard E, Korablev O, Bertaux J-L (2009) Preliminary characterization of the upper haze by SPICAV/SOIR solar occultation in UV to mid-IR onboard Venus Express. J Geophys Res 114:E00B42
Wilquet V, Drummond R, Mahieux A, Robert S, Vandaele AC, Bertaux J-L (2012) Optical extinction due to aerosols in the upper haze of Venus: four years of SOIR/VEX observations from 2006 to 2010. Icarus 217:875–881
Zhang Xi, Liang M, Mills F, Belyaev D, Yung Y (2012) Sulfur chemistry in the middle atmosphere of Venus. Icarus 217:714–739

Publisher's Note